Mapping gigahertz vibrations in a plasmonic–phononic crystal

New Journal of Physics

Mapping gigahertz vibrations in a plasmonic–phononic crystal

Timothy A Kelf[1]**, Wataru Hoshii**[1]**, Paul H Otsuka**[1]**,
Hirotaka Sakuma**[1]**, Istvan A Veres**[2]**, Robin M Cole**[3]**,
Sumeet Mahajan**[3]**, Jeremy J Baumberg**[3]**, Motonobu Tomoda**[1]**,
Osamu Matsuda**[1] **and Oliver B Wright**[1,4]

[1] Division of Applied Physics, Faculty of Engineering, Hokkaido University, Sapporo 060-8628, Japan
[2] Research Center for Non-Destructive Testing GmbH, Altenberger Straße 69, A-4040 Linz, Austria
[3] Nanophotonics Centre, Cavendish Laboratory, University of Cambridge, Cambridge CB3 OHE, UK
E-mail: olly@eng.hokudai.ac.jp

Abstract. We image the gigahertz vibrational modes of a plasmonic–phononic crystal at sub-micron resolution by means of an ultrafast optical technique, using a triangular array of spherical gold nanovoids as a sample. Light is strongly coupled to the plasmonic modes, which interact with the gigahertz phonons by a process akin to surface-enhanced stimulated Brillouin scattering. A marked enhancement in the observed optical reflectivity change at the centre of a void on phononic resonance is likely to be caused by this mechanism. By comparison with numerical simulations of the vibrational field, we identify resonant breathing deformations of the voids and elucidate the corresponding mode shapes. We thus establish scanned optomechanical probing of periodic plasmonic–phononic structures as a new means of investigating their coupled excitations on the nanoscale.

⑤ Online supplementary data available from stacks.iop.org/NJP/15/023013/mmedia

[4] Author to whom any correspondence should be addressed.

IOP Institute of Physics Φ DEUTSCHE PHYSIKALISCHE GESELLSCHAFT

Contents

1. Introduction

The study of the gigahertz acoustic vibrations of nanostructures and nano-objects using ultrafast optical techniques has developed rapidly in parallel with the progress in nanofabrication. The drive to better understand vibrational modes of nanostructures, in particular their frequency and damping, stems from the dependence of these properties on geometry [1–4], as well as from possible applications in ultrasensitive mass, chemical or gas sensing [5–7]. In particular, attention has been devoted to periodic acoustic nanostructures, i.e. phononic crystals, where phononic band gaps arise [8–16]; such research on regular arrays of nano-objects has led to enhanced control over systems with resonant frequencies in the gigahertz range, paving the way for the development of novel high-frequency acoustic devices such as acousto-optic modulators and sensors.

The optical properties of periodic nanostructures have also come under scrutiny. In particular, for metallic samples it is the plasmonic properties, i.e. involving electromagnetic coupling to charge-density oscillations, that show great promise because of their applications in photonic nanocircuits, surface-enhanced Raman scattering (SERS) and sensing [17–20]. The harnessing of *both* plasmonic and phononic effects in periodic metallic nanostructures, i.e. plasmonic crystals, is a relatively new field: following on from research into the vibrations of individual or small groups of plasmonic nano-objects [21–28], gigahertz vibrations of gratings and hole arrays exhibiting surface-plasmon-mediated extraordinary optical transmission have been studied [29, 30], as well as such vibrations in three-dimensional arrays of spherical nanoshells [10, 31]. However, no attention has been paid to the coupling of the plasmonic properties with the collective phononic properties of a periodic nanostructure in the time domain.

In this paper we extend these investigations to probe the coupling of the plasmonic and phononic properties of periodic solids, or what may conveniently be termed *plasphonic* properties, in an array of gold nanovoids. These structures, consisting of truncated spherical voids, have previously been shown to have pronounced plasmonic properties [32–35], leading to enhanced Raman scattering [18] and fluorescence [36]. To understand the interaction of gigahertz vibrational modes and plasmonic modes in periodic structures, an optimal technique would be to probe the vibrational field over the sample. Here we exploit an imaging technique based on ultrafast optics to excite a periodic structure in the form of a nanovoid plasmonic
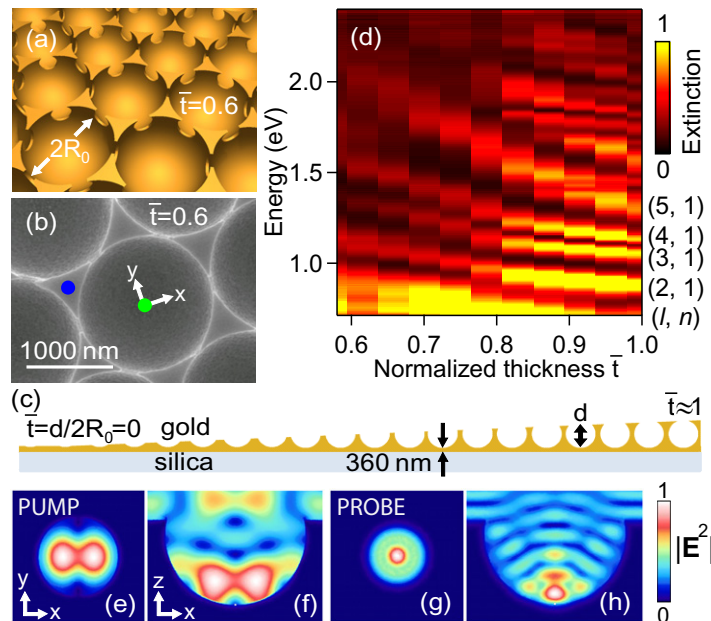
Figure 1. (a) Schematic diagram of the sample with void radius $R_0 = 800$ nm at normalized thickness $\bar{t} = 0.6$, with (b) a scanning electron microscope image. The blue and green spots correspond to specific measured points. (c) Schematic cross section of the sample showing the change in $\bar{t}$ with position. (A Cr adhesion layer is not shown.) (d) Normal-incidence normalized experimental optical extinction spectrum of the $R_0 = 800$ nm sample for a range of $\bar{t}$. Mie-plasmon mode-number assignments at $\bar{t} = 1$ are given on the right. (e), (f) Simulated spatial intensity distributions of the optical field $|\mathbf{E}^2|$ inside the void for normally incident plane-wave x-polarized pump light at 820 nm focused on the centre of a single, isolated void with $\bar{t} = 0.6$. (e) Top view (xy-plane cross section through the points for which the intensity is a maximum) and (f) side view. The length scales in (e) and (f) are identical, and the intensity scales are normalized. (g), (h) Equivalent intensity distributions for circularly polarized plane-wave probe light at 410 nm.

crystal, and make two-dimensional spatially resolved measurements of transient reflectivity changes. We thereby obtain, for what to our knowledge is the first time, images representing the plasphonic response of a plasmonic–phononic crystal, and demonstrate a marked enhancement in the optical reflectivity change on phononic resonance for optical excitation in the centre of a nanovoid. We interpret our results by means of acoustic simulations.

2. Experiments and results

2.1. Samples

The gold nanovoid arrays are formed in triangular lattices using a nano-casting process involving electrochemical deposition on a silica substrate of thickness 1 mm through a template of self-assembled latex spheres (for details see [35]). Retracting the sample from a plating solution allows a graded thickness geometry to be achieved on a single sample. A three-dimensional rendering of a void array is shown in figure 1(a), showing their truncation.

A scanning electron microscope image is shown in figure 1(b) for a void radius of $R_0 = 800$ nm, a pitch of 1580 nm and a truncation thickness d of 960 nm, or normalized thickness $\bar{t} = d/(2R_0) = 0.6$. The quantity $\bar{t}$ varies (over a few mm) from 0 at the thin end of the sample to 1 at the thick end, as shown schematically in figure 1(c) together with the definition of d. There is a 360 nm layer of gold below the voids deposited onto a 25 nm chromium adhesion layer on the silica substrate. When $\bar{t}$ is small the surface takes the form of an array of shallow dishes. For larger values of $\bar{t}$, triangular pillars exist between three adjacent truncated spherical cavities, as in the case of $\bar{t} = 0.6$ (figures 1(a) and (b)). At larger values of $\bar{t}$ these pillars are connected and, for $\bar{t} \geqslant 1$, the sample consists of an array of connected spherical voids. We conduct ultrafast optical experiments on this sample at a position corresponding to $\bar{t} = 0.6$, where the vibrational modes are clearly detected.

2.2. Optical setup and characterization

We use a two-colour, pump–probe technique to excite and probe the gigahertz vibrational modes of the sample. A Ti:sapphire mode-locked laser with a central wavelength of 820 nm, a pulse duration of 200 fs and a repetition rate of 81 MHz is used to form a linearly polarized pump beam for excitation with incident pulse energy 0.4 nJ. (We verified that the optical reflectivity changes were proportional to the pulse energy up to this value.) The pump polarization is aligned along the x-direction (i.e. a symmetry direction) of the nanovoid lattice in figure 1. The pump beam is modulated by an acousto-optic modulator at 1.1 MHz before being focused at normal incidence through a $\times 100$ objective to a full-width at half-maximum intensity 650 nm diameter spot on the sample. The choice of $R_0 = 800$ nm thus allows us to excite a single plasmonic void (without damage). This point-like source results in a large number of vibrational modes with a wide range of acoustic wavevectors **k** being excited [37]. These nanovoid samples also support a number of localized and extended plasmonic modes [32–35]: the former, termed Mie plasmons, are characterized by angular and principal mode numbers l and n; the latter, termed Bragg plasmons, are characterized by associated reciprocal lattice vectors. In the present experiments at normal optical incidence, we expect localized Mie plasmons to have a strong influence on the optical absorption. The tight optical focusing, however, implies that wavevectors corresponding to propagating modes inside the plasmonic Brillouin zone are also excited. The white-light-measured normalized optical absorption spectrum for the $R_0 = 800$ nm sample for a range of normalized thicknesses $\bar{t}$, shown in figure 1(d), shows clearly the excitation of Mie-like plasmons [32–35]. By extrapolation from previous published data [34, 35] for voids of radius 300 and 500 nm, we identify at the side of the figure the modes corresponding to $n = 1$, $l = 1$–4 for the analytically solvable case of $\bar{t} = 1$ (the case of a spherical cavity in gold). To show the field localization produced by Mie-like plasmon modes, the optical intensity distribution produced by linearly polarized plane-wave incidence at the pump wavelength is extracted from electromagnetic finite-element simulations (COMSOL Multiphysics—using standard optical parameters for gold [38]) in figures 1(e) and (f) for a single nanovoid of radius $R_0 = 800$ nm and $\bar{t} = 0.6$. Concentration of the electric field near the bottom of the void is evident.

We have previously shown that two-colour pump–probe techniques are ideally suited to spatially resolve GHz vibrational distributions [37]. A frequency-doubled probe beam at $\lambda = 410$ nm (pulse energy 0.04 nJ) is passed through a delay line, is directed onto the sample through a quarter-wave plate to render it circularly-polarized, through a dichroic mirror to combine it with the pump beam, and then through the same objective as the pump to focus

it, and is focused to the same spot size, at the same point on the sample and in the same focal plane as the pump (i.e. confocally). The pump–probe focusing plane was chosen at a point ∼400 nm below the top plane of the sample, a plane for which the sample features were well resolved. (See below for images.) Both pump and probe spot sizes were controlled by spatial filters in the respective beams. The simulated optical intensity distribution produced by circularly-polarized plane-wave incidence at the probe wavelength is shown in figures 1(g) and (h), indicative of higher-order Mie-like-plasmon excitation compared to the pump because of the higher photon energy. Owing to the circular polarization, the intensity distribution possesses circular symmetry. Similar plots for other void diameters, truncations and wavelengths are given elsewhere [34, 35]. The reflected probe light is detected after reflection from a polarizing beam splitter and compared with that of a reference beam using a balanced photodiode. Synchronous lock-in detection is then used to detect the small, $\sim 10^{-4}$, relative variations in intensity of the probe light as a function of the pump–probe delay time.

2.3. Results for selected points on the sample

Figure 2(a) shows the relative probe reflectivity change $\delta R/R$ for two different (high-symmetry) points on the nanovoid lattice. The green curve corresponds to the centre of a void (green dot in figure 1(b)—identified in experiment from their higher reflectivity), whereas the blue curve corresponds to a 'pillar point' equidistant between three voids (blue dot in figure 1(b)). The void-centre trace and pillar traces were averaged over 7 and 24 equivalent locations on the void array, respectively[5]. At delay time $t = 0$, the pump beam excites electrons in the gold, prompting a rapid increase in reflectivity. Within ∼500 fs the electrons thermalize [39], and the energy is transferred to the phonons, heating the sample. This heating also produces a corresponding complex refractive index change, leading, in general, to an impulsive response of $\delta R/R$.[6] This heating excites the vibrational modes of the sample through thermal expansion, producing oscillations in $\delta R/R$.

These oscillations are sensed by the frequency shifts of the plasmon resonance and also by the modulation in the spatial intensity distribution of the returning probe beam (induced lensing). Both these effects are induced by the changes in shape of the oscillating nanostructure. (The photoelastic effect, i.e. the direct modulation of the refractive index of the gold by the strain in the sample, is negligible at the chosen probe wavelength [40].) These detection mechanisms are extremely sensitive to the way the probe light scatters from the sample surface.

The temporal variation can be analysed within the time window of 12.3 ns allowed by the optical pulses (which repeat with this period). To obtain the response of the sample in the frequency domain, we perform a temporal Fourier transform over this window (after first zero padding to $t = -12.3$ ns for smoothing purposes, subtracting the background variation with an exponential curve, and removing thermal spikes by setting the first 30 ps of the variation to a constant value). The result is shown in figure 2(b) for the two chosen high-symmetry points on

---

[5] The seven voids and 24 pillars correspond to those enclosed by the hexagon in figure 3(a).

[6] The calculated maximum transient temperature change of a flat gold film under the same excitation conditions is ∼70 K, assuming that the electron diffusion depth is ∼100 nm [51]. Our observed value for $\delta R/R \sim 5 \times 10^{-4}$ (see figure 2(a)) arising from this temperature change is in approximate agreement with that, $\sim 10^{-3}$, estimated from available data for the thermoreflectance of gold at the probe photon energy [52]. Under these conditions the steady-state average temperature rise of the surface of a thin gold film on a silica substrate in the centre of the pump-light spot is estimated to be ∼150 K.
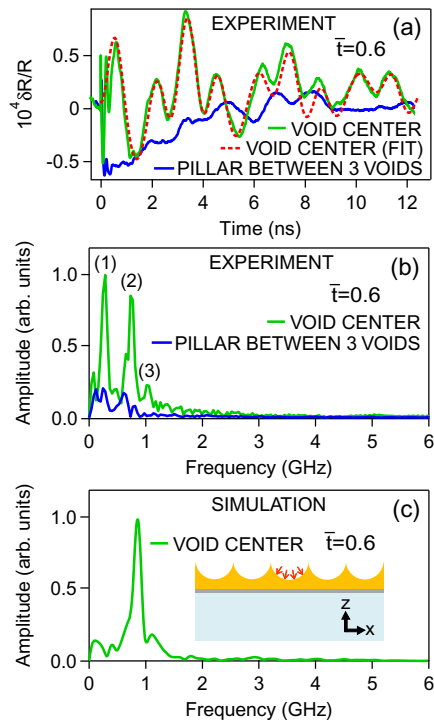
Figure 2. (a) Solid curves: measured induced optical reflectivity ($\delta R/R$) versus delay time t. Pump and probe beams focused at the void centre (green curve, on green spot in figure 1(b)) and pillar between three voids (blue curve, on blue spot in figure 1(b)). Dashed curve (red): fit to the void-centre data. (b) Modulus of the temporal Fourier transform of the experimental induced reflectivity variation versus frequency for the void centre (green) and pillars (blue), plotted on the same scale. (c) Simulated modulus of the temporal Fourier transform of the z-directed displacement at the surface of the sample versus frequency for impulsive excitation at the void centre. Inset: schematic diagram of the model used for acoustic simulations, showing the directions of the impulsive force vectors (red arrows).

the sample. A number of vibrational resonances are observed at the void centre: in this position there are clearly visible peaks at 0.28, 0.73 and 1.01 GHz,[7] whereas for the pillars between three voids the response is much weaker, with peaks in the same range. In particular, for 0.73 GHz the response is $\sim$120 times smaller at the pillar compared to the void centre. The larger response for excitation in the void centre we believe to be mainly the result of a more efficient excitation of the void vibrations and a more efficient modulation of the probe beam. Both these effects are enhanced by the excitation of Mie-like plasmons.

The overall decrease in the modulus of the temporal Fourier transform (|FT|) of δR with frequency is presumably caused by a decrease in the detection efficiency when the dominant acoustic wavelength associated with the modes of vibration of the sample becomes smaller than the optical spot size. For a wavelength of $\sim$600 nm and a characteristic surface acoustic wave velocity of $\sim$1.3 km s^{-1} noted in our simulations, as shown in the supplementary data

---

[7] Mode (2) has, in fact, a reproducible shoulder, suggesting that a second lower-amplitude mode at a slightly lower frequency also exists near 0.65 GHz.

Table 1. Values for the parameters used to fit the experimental data for the reflectivity variation to a sum of damped sinusoidal waves: (1)–(3) refer to the three main experimental resonance peaks.

Mode	(1)	(2)	(3)
Frequency (GHz)	0.27	0.75	1.01
Relative amplitude	1	0.91	0.25
Q-factor	6.5	19	30
Phase (ψ/π)	0.22	−0.93	−0.75

(available from stacks.iop.org/NJP/15/023013/mmedia), this corresponds to a cutoff frequency of $\sim$2 GHz. (Minor experimental resonances are visible up to around this frequency.) A similar cutoff was recently noted for vibrations of nanorings [27].

In order to extract the experimental frequencies f, Q-factors and phases ψ for the three main vibrational resonances, the experimental time-domain data for the void centre are fitted to a set of three damped sinusoidal waves of arbitrary phase, amplitude and damping, adjusted for each resonance (labelled by index i) so as to minimize the mean absolute difference between the data and the fitting function

$$\delta R(t) = \sum_{i=1}^{3} A_i \cos(2\pi f_i t + \psi_i) \exp(-\gamma_i t/2), \tag{1}$$

where $\gamma_i = 2\pi f_i / Q_i$ and Q_i is the corresponding Q-factor.[8] Table 1 shows the resulting fitted parameters obtained for each of the experimentally detected modes. The fitted frequencies correspond closely to the experimentally measured peak positions, and the fit in the time domain, shown by the dashed green line in figure 2(a), gives good agreement with that observed. This fitting procedure is subject to errors of up to $\sim$10% in the obtained parameters (with the phase compared to 2π).

The fitted frequencies are 0.27, 0.75 and 1.01 GHz, labelled by (1), (2) and (3), respectively. The observed Q-factors, in the range 6–30 (or mode lifetimes all $\sim$100 ns), are strongly influenced by surface acoustic wave radiation and leakage to the bulk, as discussed later, and also possibly by inhomogeneous broadening owing to sample defects[9].

The phase lead ψ for each of the modes is shown in table 1 in units of π. If the excitation of thermal stress is considered instantaneous on a time scale compared to the oscillation period, the nanovoids should start oscillating from a point of maximum displacement, yielding a cosine variation in displacement [41, 42]. This is indeed approximately the case for the mode (2). Deviations from such a variation can occur owing to thermal diffusion in the gold or silica substrate, as previously observed in ultrafast vibrations of metal nanoshells and nanorings [27, 43]. The sign of ψ also depends on the optomechanical detection mechanism, such as, for example, the spatial distribution of the modulated light reflected from the nanovoid and its passage through the detection optics.

---

[8] In [16, 27], the factor of 1/2 was inadvertently not included in the exponential corresponding to equation (1) in the present paper, although the values of Q are accurate in those reports.

[9] However, the resonance peak widths for the data for a single void are approximately the same as that of the average of seven voids.
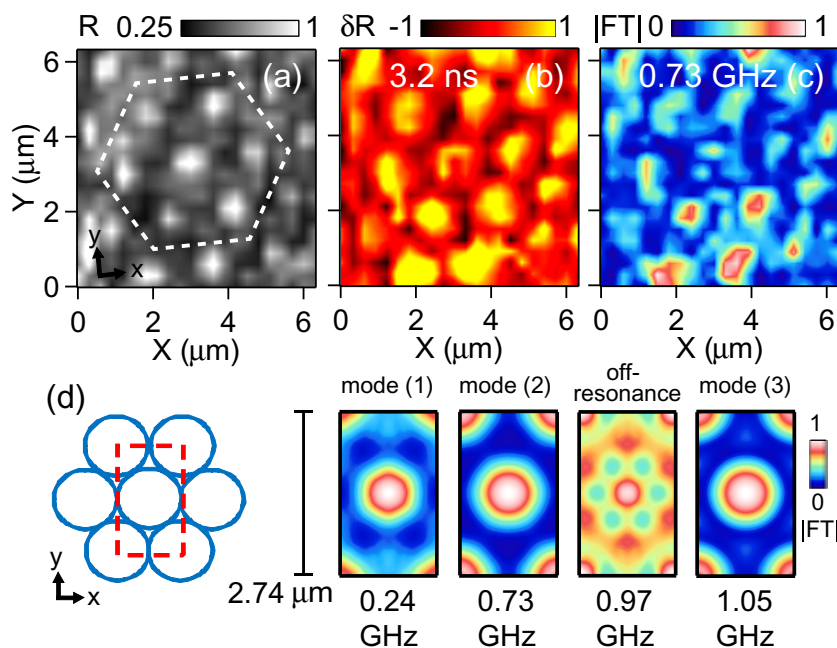
Figure 3. (a) Image of the reflectivity of the sample at the 410 nm probe wavelength scanned along the X, Y directions (tilted with respect to the x- and y-axes of the lattice). The higher-reflectivity regions correspond to the void centres. The dashed hexagon encloses the seven central voids in this image. (b) Corresponding normalized image for the change in reflectivity δR at delay time $t = 3.2$ ns. (c) Normalized modulus of the temporal Fourier transform (|FT|) of δR at 0.73 GHz. (d) Averaged normalized modulus of the temporal Fourier transform at four different frequencies for the rectangular region shown by the red dashed lines in the inset. In (d) the average was taken over regions around the seven central voids.

2.4. Ultrafast imaging

To better visualize the nanovoid vibrations, the sample is mounted on a closed-loop-control piezoelectric stage with 10-nm spatial resolution. We map the vibrational response in steps of 300 nm over a 6.3 μm square region. A typical probe reflectivity (R) image is shown in figure 3(a). This normalized image and subsequent images in figure 3 are smoothed to remove graininess. The centres of the voids correspond to the bright white regions, whereas the pillars, in spite of their sub-micron size, show up as the smaller, grey spots in between[10]. The ratio between the reflectivity R at these points is $\sim$1:0.6 (with the darkest regions taking the value $\sim$0.25 on this scale). Figure 3(b) shows an image of the change in probe reflectivity $\delta R(t)$ at delay time $t = 3.2$ ns. The position of the nanovoid centres is again clearly visible. (An animation of this temporal response is given in the supplementary data, available from stacks.iop.org/NJP/15/023013/mmedia.)

---

[10] The few off-symmetry features are caused by sample defects.

These data allow one to construct spatially- and frequency-resolved images of the modulus of the temporal Fourier transform in steps of the optical repetition frequency 0.081 GHz.[11] An image for 0.73 GHz, corresponding to mode (2), is shown in figure 3(c). Regions of stronger δR correspond to the nanovoid centres in this image, which shows some random variation from void to void (partly due to the finite step in the spatial scan). Using the point symmetry of the lattice[12] allows us to average the complex Fourier transform over six-fold rotation and reflection, and spatially around each void position using the seven central voids (see figure 3(a))[13]. We thus present the mean response for |FT| over a rectangular cell centred on a nanovoid, as shown in figure 3(d) for modes (1)–(3), as well as for another frequency for comparison. For modes (1)–(3), (represented by frequencies 0.24, 0.73 and 1.05 GHz in the images, respectively) the response in the central region in the void is characteristically greater than that in between, as mentioned above for mode (2). Because the Fourier transform phase is also available, these images can be seen in animation (see the supplementary data, available from stacks.iop.org/NJP/15/023013/mmedia). Mode (1) corresponds to a wavevector inside the first Brillouin zone of the phononic lattice, whereas wavevectors for modes (2) and (3) lie outside (see the supplementary data).

Although our probe spot diameter of 650 nm limits the available resolution, we were able to reproducibly detect a significantly different spatial response at 0.97 GHz, just below mode (3) resonance, also shown in figure 3(d): δR near the pillar positions between three voids is very similar to that near the void centres. (Slight deviations from lattice translational symmetry are caused by sample imperfections and possibly by the finite step size of the raster scan.) These off-void-centre responses confirm our conclusions from point-by-point measurements that the flat pillar tops are also effective for sample excitation at certain frequencies. Excitation at the side of a void in an off-symmetry position on the plasmonic–phononic crystal is expected to involve complex optical fields spread out within a void, as suggested by previous models [34], and these excitation positions appear to be less effective in inducing a response in δR, either because of less efficient optical excitation of vibrations, less efficient probe-beam optomechanical coupling or the smaller reflectivity R.

The spectrum of figure 1(d) (for $\bar{t} = 0.6$) shows that our pump wavelength is tuned close to a plasmonic resonance. Although our probe wavelength is not covered by this spectrum, extrapolation of the data of figure 1(d) to shorter wavelengths suggests that this wavelength is also likely to lie close to a plasmonic resonance. This proximity to plasmonic resonances suggests that plasmonic enhancement of the excitation and detection of the acoustic phonon response is involved here, in particular for mode (2) of the void centre where the very strong

---

[11] For the image data, we did not subtract the background because each trace showed increased noise compared to the averaged traces in figure 2(a). This does not significantly affect the images. With zero padding one can obtain a frequency resolution of 0.0405 GHz, but this was not used in the image analysis in order to avoid extra interpolation.

[12] Thermal diffusion serves to redistribute the heat generated by optical absorption during the thermoelastic generation of vibrations. The thermal diffusion length in gold over a typical vibrational cycle $T = 1$ ns is $\sim\sqrt{DT} \sim 400$ nm, where $D \approx 1.3 \times 10^{-4}$ m^2 s^{-1} is the thermal diffusivity of gold. We therefore assume that the spatial distribution of thermal expansion effective in generating the vibrational field produced by the linearly polarized pump beam does not break the point symmetry of the lattice.

[13] Averaging was carried out by rotation and reflection of regions of dimensions 1.6 μm × 1.6 μm centred on each void. This forces six-fold rotational symmetry about the centre of the processed images and six axes of reflection, but does not force the translational symmetry of the lattice.

enhancement in δR ($\sim$120) is observed (and also in $\delta R/R$, $\sim$70) compared to that of the pillar (that appears to be non-resonant at this frequency). Excluding the void-centre vibrational-resonance enhancement factor of $Q \approx 20$ for this mode (see table 1), this suggests a factor $\sim$6 enhancement in δR. Plasmon-mediated signal enhancements are observed in SERS [44–48], and related enhancements in the case of coherent acoustic phonons can be termed surface-enhanced stimulated Brillouin scattering (SESBS) by analogy to the non-stimulated version SEBS (for which thermally-excited incoherent phonons provide the scattering source) [49, 50]. By analogy with SERS or SEBS, the enhancement in SESBS depends on the plasmon-enhanced optical amplitudes at the pump and probe wavelengths. Here the detection mechanism differs from conventional Brillouin scattering in that it takes place in the time domain, and is manifested by a heterodyne beating between the Brillouin-scattered and reflected probe light. The complex and different nature of the optical scattering of the tightly focused optical probe beam from the void-centre and pillar points, however, prevents us from definitively identifying the origin of the enhancement in the present study. (This will have to await optically spectrally resolved measurements on this type of sample in order to scan through plasmonic resonances.) A full numerical analysis of such spatio-temporal effects involving optical excitation and detection at arbitrary points across the sample is very involved, and requires a knowledge of the plasmonic dispersion [33] characteristics of the structure. This is beyond the scope of this paper, so we concentrate here mainly on the void-centre response.

3. Acoustic simulations and analysis

To interpret the resonant frequencies at the void centre, we have carried out numerical elastic simulations with a time-domain finite-element method. We use the model shown in cross section in the inset of figure 2(c), including the gold structure, chromium underlayer and substrate. The excitation is approximated by an impulsive force distributed uniformly over a 1 μm diameter at the bottom of the void and normal to the surface. The functional form of the force is taken to be a quarter of a sine wave for a duration of 80 ps, providing a vibrational spectrum similar to that in experiment. The frequencies obtained are rather insensitive to the exact nature of the excitation for a given rise time of the impulse (for further details see the supplementary data, available from stacks.iop.org/NJP/15/023013/mmedia). The amplitude of the z-directed displacement at the centre of a void is plotted by calculating the modulus of the temporal Fourier transform (over the time period equal to that of the laser repetition), as shown in figure 2(c). A dominant peak is predicted near 0.89 GHz, close to the 0.73 GHz peak (mode (2)) in the experiment. A smaller peak at 1.05 GHz, close to the corresponding experimental mode (3) peak position, is also seen. However, the experimental mode (1) peak at 0.28 GHz does not appear. The height of the peaks in experiment is not expected to correspond to the simulation because of the neglect of the details of the optical excitation and detection mechanisms, and differences in frequency may be caused by slight deviations of the model from the real sample geometry and mechanical properties. The narrower main peak in the simulation (corresponding to $Q \sim 70$) may be a result of the absence of sample defects or the effect of the approximate acoustic source used. As observed in experiment, some smaller resonances are predicted between 1 and 3 GHz. A specific, partly-longitudinal thickness resonance is also predicted near 4 GHz (see the supplementary data).

    In order to better understand the main resonance peak in the simulation, we have plotted the associated acoustic fields and deformations in figure 4. The amplitudes of the deformations (figure 4(a)) are obtained from the modulus of the temporal Fourier transform at 0.89 GHz, for
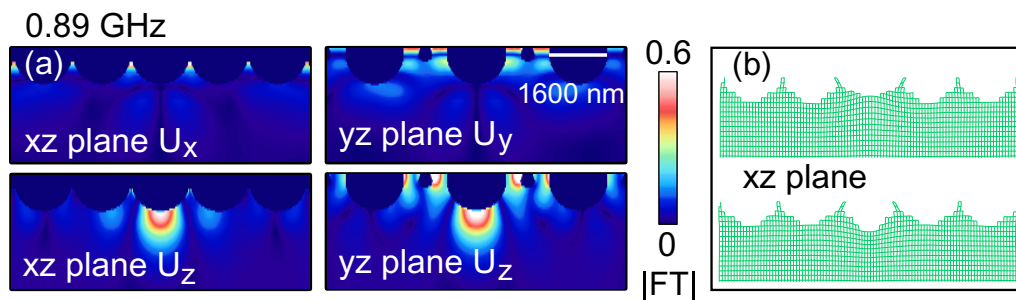
Figure 4. (a) Simulated images of the normalized modulus of the temporal Fourier transform (|FT|) of the sample displacement, when excited around a void centre, viewed in cross section at frequency $f = 0.89\,\text{GHz}$. The relative magnitudes of the displacements are accurately represented in the set of four plots, which are normalized to a maximum of 1. (b) Deformations at times $1/(2f)$ (π out of phase) for the xz plane. All cross sections are taken through the centre of a void.

two perpendicular cross sections through the sample for various displacement components U_j, with $j = x$, y or z. This vibrational mode is characterized by a significant deformation U_z at the bottom of the void and significant in-plane deformations around the rims of the excited void. This is more clearly seen in the maps of figure 4(b), showing breathing deformations for the xz plane at times separated by half a period. (The motion can be viewed as an animation in the supplementary data together with a plot in the xy plane.) The vibrations involve a transient change in the radius of curvature of the void, thus shifting the resonance frequencies of the Mie-like plasmons and the spatial intensity distribution of the returning beam, as previously mentioned, and allowing the vibrations to be detected.

A rough estimate of this contribution to the probe reflectivity modulation from the shift in the plasmon resonance can be made as follows: $\delta R = dR/d\omega_0 \ d\omega_0/dR_0 \ \delta R_0$, where ω_0 is the angular frequency of the plasmonic resonance closest to that of the probe beam and δR_0 is the vibrationally induced change in the radius R_0. As an approximation which applies for our void radii, $\omega_0 = K/R_0$, where K is a constant depending on the mode numbers and frequency of the Mie-like resonance involved. Therefore $\delta R = -dR/d\omega_0 \ K \ \delta R_0/R_0^2$. The detection efficiency in this case can be enhanced if the probe wavelength is just off a plasmon resonance, which is likely to be the case in our experiment[14]. Similar considerations apply to the other vibrational frequencies where the void radius is modulated (see plots for U_j and for their deformation, as well as animations, in the supplementary data, available from stacks.iop.org/NJP/15/023013/mmedia). It is clear from these plots and animations that significant acoustic energy leaks into the bulk. It is this coupling of the surface-propagating acoustic modes and the substrate modes that is partly responsible for the relatively low acoustic Q-factors that we observe in experiment. Although we have considered a single void array, a wide range of nanostructural design parameters for void arrays are available to enhance the effect of the change in void radius on the plasmonic reflectivity, in a similar way to the enhancements achieved in SERS or SEBS.

---

[14] $dR(\omega)/d\omega_0 \sim R(\omega_0)Q_0/\omega_0$ for a Mie resonance with an optical Q-factor equal to Q_0, where ω is the probe angular frequency. For our nanovoid sample, $Q_0 \sim 10\text{–}20$—see figure 1(d).

IOP Institute of Physics ⏀ DEUTSCHE PHYSIKALISCHE GESELLSCHAFT

4. Discussion and conclusions

Clearly, a number of interesting questions arise from this study. How does the acoustic displacement field in the sample depend on the source position generating the initial plasmons? What nano-optics is involved in the probe interaction and reflection from the sample, and how is the optical modulation influenced by the detection optics? What is the exact role of the localized plasmonic resonances on both excitation and detection? What is the influence of the propagating plasmonic modes of the plasmonic crystal that makes up the periodic textured sample? To answer these questions, further studies and simulations of the interaction of light with the deformed surface should be carried out to investigate the coupling of the acoustic and plasmonic fields on the nanoscale. Our results represent a challenge for rigorous interpretation and also a stimulus for further experimentation in this unexplored field of research.

In conclusion, the vibrational modes of a plasmonic–phononic crystal have been experimentally mapped for the first time in both the temporal and frequency domains. The use of tightly-focused confocal pump and probe beams in our gold nanovoid array allows the sub-micron spatially-resolved vibrational response of the sample at each point to be assessed, highly dependent on the plasmonic response at the pump and probe wavelengths as well as on the phononic response. Observed acoustic breathing resonances of the voids near 0.7 and 1 GHz are reasonably well accounted for by numerical simulations based on impulsive force excitation. We also note a marked enhancement of reflectivity changes in the centre of a nanovoid for the resonance near 0.7 GHz. Such observations, involving spatial mapping of the SESBS, are analogous to the mapping of plasmonic and molecular systems with SERS or SEBS. The complexity of the nanoscale geometry and its strong influence on the confined electromagnetic and acoustic waves provide a wide range of avenues for sample optimization: an exciting line of future research would be to tailor both the plasmonic and phononic band structures to enhance the resonant plasphonic interactions, thereby opening up the possibility of novel devices such as acousto-optic modulators. Our approach for direct spatial mapping of the optomechanical interactions in plasmonic–phononic crystals should prove vital to the verification and characterization of such devices.

References

[1] Antonelli G A, Maris H J, Malhotra S G and Harper J M E 2002 *J. Appl. Phys.* **91** 3261
[2] Hu M, Wang X, Hartland G V, Mulvaney P, Juste J P and Sader J J E 2003 *Am. Chem. Soc.* **125** 14925
[3] Kuok M H, Lim H S, Ng S C, Liu N N and Wang Z K 2003 *Phys. Rev. Lett.* **90** 255502
[4] Hartland G V 2011 *Chem. Rev.* **111** 3858
[5] Yang Y T, Callegari C, Feng X L, Ekinci K L and Roukes M L 2006 *Nano Lett.* **6** 583
[6] Li M, Tang H X and Roukes M L 2007 *Nature Nanotechnol.* **2** 114

[7] Pelton M, Sader J E, Burgin J, Liu M, Guyot-Sionnest P and Gosztola D 2009 *Nature Nanotechnol.* **4** 492

[8] Robillard J-F, Devos A, Roch-Jeune I and Mante P A 2008 *Phys. Rev.* B **78** 064302

[9] Giannetti C *et al* 2007 *Phys. Rev.* B **76** 125413

[10] Mazurenko D A, Shan X, Stiefelhagen J C P, Graf C M, Van Blaaderen A and Dijkhuis J I 2007 *Phys. Rev.* B **75** 161102

[11] Taubert R, Hudert F, Bartels A, Merkt F, Habenicht A, Leiderer P and Dekorsy T 2007 *New J. Phys.* **9** 376

[12] Akimov A V, Tanaka Y, Pevtsov A B, Kaplan S F, Golubev V G, Tamura S, Yakovlev D R and Bayer M 2008 *Phys. Rev. Lett.* **101** 033902

[13] Yamaguchi M, Liu D Y J and Lu T-M 2009 *J. Appl. Phys.* **106** 033517

[14] Wen Y-C, Sun J-H, Dais C, Grützmacher D, Wu T-T, Shi J-W and Sun C-K 2010 *Appl. Phys. Lett.* **96** 123113

[15] Marty R, Arbouet A, Girard C, Mlayah A, Paillard V, Lin V, Teo S L and Tripathy S 2011 *Nano Lett.* **11** 3301

[16] Sakuma H, Tomoda M, Otsuka P H, Matsuda O, Wright O B, Fukui T, Tomioka K and Veres I A 2012 *Appl. Phys. Lett.* **100** 131902

[17] Malyarchuk V, Hua F, Mack N H, Velasquez V T, White J O, Nuzzo R G and Rogers J A 2005 *Opt. Express* **13** 5669

[18] Baumberg J J, Kelf T A, Sugawara Y, Cintra S, Abdelsalam M E, Bartlett P N and Russell A E 2005 *Nano Lett.* **5** 2262

[19] Baudrion A L, Weeber J C, Dereux A, Lecamp G, Lalanne P and Bozhevolnyi S I 2006 *Phys. Rev.* B **74** 125406

[20] Tao A R, Ceperley D P, Sinsermsuksakul P, Neureuther A R and Yang P 2008 *Nano Lett.* **8** 4033

[21] Nelet A, Crut A, Arbouet A, Fatti N D, Vallée F, Portales H, Saviot L and Duval E 2004 *Appl. Surf. Sci.* **226** 209

[22] Margueritat J, Gonzalo J, Afonso C, Mlayah A, Murray D B and Saviot L 2006 *Nano Lett.* **6** 2037

[23] Burgin J, Langot P, Arbouet A, Margueritat J, Gonzalo J, Afonso C N, Vallée F, Mlayah A, Rossell M D and Van Tendeloo G 2008 *Nano Lett.* **8** 1296

[24] Zijlstra P, Tchebotareva A L, Chon J W M, Gu M and Orrit M 2008 *Nano Lett.* **8** 3493

[25] Large N, Saviot L, Margueritat J, Gonzalo J, Afonso C N, Arbouet A, Langot P, Mlayah A and Aizpurua J 2009 *Nano Lett.* **9** 3732

[26] Tripathy S, Marty R, Lin V K, Teo S L, Ye E, Arbouet A, Saviot L, Girard C, Han M and Mlayah A 2011 *Nano Lett.* **11** 431

[27] Kelf T A, Tanaka Y, Matsuda O, Larsson E, Sutherland D S and Wright O B 2011 *Nano Lett.* **11** 3893

[28] Schumacher T, Kratzer K, Molnar D, Hentschel M, Giessen H and Lippitz M 2011 *Nature Commun.* **2** 333

[29] Gérard D, Laude V, Sadani B, Khelif A, Van Labeke D and Guizal B 2007 *Phys. Rev.* B **76** 235427

[30] Le Guyader L, Kirilyuk A, Rasing T, Wurtz G A, Zayats A V, Alkemade P F A and Smolyaninov I I 2008 *Phys J. D: Appl. Phys.* **41** 195102

[31] Huang W Y, Qian W and El-Sayed M A 2008 *Adv. Mater.* **20** 733

[32] Coyle S, Netti M C, Baumberg J J, Ghanem M A, Birkin P R, Bartlett P N and Whittaker D M 2001 *Phys. Rev. Lett.* **87** 176801

[33] Kelf T A, Sugawara Y, Baumberg J J, Abdelsalam M and Bartlett P N 2005 *Phys. Rev. Lett.* **95** 116802

[34] Kelf T A, Sugawara Y, Cole R M, Baumberg J J, Abdelsalam M E, Cintra S, Mahajan S, Russell A E and Bartlett P N 2006 *Phys. Rev.* B **74** 245415

[35] Cole R M, Baumberg J J, De Abajo F J G, Mahajan S, Abdelsalam M and Bartlett P N 2007 *Nano Lett.* **7** 2094

[36] Sugawara Y, Kelf T A, Baumberg J J, Abdelsalam M E and Bartlett P N 2006 *Phys. Rev. Lett.* **97** 266808

[37] Profunser D M, Muramoto E, Matsuda O, Wright O B and Lang U 2009 *Phys. Rev.* B **80** 014301

[38] Johnson P B and Christy R W 1972 *Phys. Rev.* B **6** 4370

[39] Sun C-K, Vallée F, Acioli L, Ippen E P and Fujimoto J G 1993 *Phys. Rev.* B **48** 365

[40] Garfinkel M, Tiemann J J and Engeler E 1966 *Phys. Rev.* **148** 695

[41] Voisin C, Fatti N D, Christofilos D and Vallée F 2000 *Appl. Surf. Sci.* **164** 131

[42] Bonacina L, Callegari A, Bonati C, van Mourik F and Chergui M 2006 *Nano Lett.* **6** 7

[43] Guillon C, Langot P, Fatti N D and Vallée F 2007 *Nano Lett.* **7** 138

IOP Institute of Physics ⟨Φ⟩DEUTSCHE PHYSIKALISCHE GESELLSCHAFT

[44] Kneipp K, Kneipp H, Itzkan I, Dasari R R and Feld M S 1999 *Chem. Rev.* **99** 2957

[45] Talley C E, Jackson J B, Oubre C, Grady N K, Hollars C W, Lane S M, Huser T R, Nordlander P and Halas N J 2005 *Nano Lett.* **5** 1569

[46] Laurent G, Felidj N, Grand J, Aubard J, Levi G, Hohenau A, Krenn J R and Aussenegg F R 2008 *J. Microsc.* **229** 189

[47] Hutchison J A, Centeno S P, Odaka H, Fukumura H, Hofkens J and Uji-i H 2009 *Nano Lett.* **9** 995

[48] Beermann J, Novikov S M, Søndergaard T, Rafaelsen J, Pedersen K and Bozhevolnyi S I 2011 *J. Opt. Soc. Am.* B **28** 372

[49] Moretti A L, Robertson W M, Fisher B and Bray R 1985 *Phys. Rev.* B **31** 3361

[50] Johnson W L, Kim S A, Utegulov Z N, Shaw J M and Draine B T 2009 *J. Phys. Chem.* C **113** 14651

[51] Wright O B 1994 *Phys. Rev.* B **49** 9985

[52] Scouler W J 1967 *Phys. Rev. Lett.* **18** 445